A New Paroxetine-Based GRK2 Inhibitor Reduces Internalization of the μ-Opioid Receptor [S]

[ID]Renee A. Bouley, [ID]Zara Y. Weinberg, Helen V. Waldschmidt, Yu-Chen Yen,
Scott D. Larsen, [ID]Manojkumar A. Puthenveedu, and [ID]John J.G. Tesmer

Life Sciences Institute (R.A.B., H.V.W.), Departments of Medicinal Chemistry (H.V.W., S.D.L.) and Pharmacology (R.A.B., Z.Y.W., M.A.P.), and Vahlteich Medicinal Chemistry Core, College of Pharmacy (H.V.W., S.D.L.), University of Michigan, Ann Arbor, Michigan; and Departments of Biological Sciences and of Medicinal Chemistry and Molecular Pharmacology (Y.-C.Y., J.J.G.T.), Purdue University, West Lafayette, Indiana

Received October 23, 2019; accepted March 18, 2020

ABSTRACT

G protein-coupled receptor (GPCR) kinases (GRKs) play a key role in terminating signals initiated by agonist-bound GPCRs. However, chronic stimulation of GPCRs, such as that which occurs during heart failure, leads to the overexpression of GRKs and maladaptive downregulation of GPCRs on the cell surface. We previously reported the discovery of potent and selective families of GRK inhibitors based on either the paroxetine or GSK180736A scaffold. A new inhibitor, **CCG258747**, which is based on paroxetine, demonstrates increased potency against the GRK2 subfamily and favorable pharmacokinetic parameters in mice. **CCG258747** and the closely related compound **CCG258208** also showed high selectivity for the GRK2 subfamily in a kinome panel of 104 kinases. We developed a cell-based assay to screen the ability of **CCG258747** and 10 other inhibitors with different GRK subfamily selectivities and with either the paroxetine or **GSK180736A** scaffold to block internalization of the μ-opioid receptor (MOR). **CCG258747** showed the best efficacy in blocking MOR internalization among the compounds tested. Furthermore, we show that compounds based on paroxetine had much better cell permeability than those based on **GSK180736A**, which explains why **GSK180736A**-based inhibitors, although being potent in vitro, do not always show efficacy in cell-based assays. This study validates the paroxetine scaffold as the most effective for GRK inhibition in living cells, confirming that GRK2 predominantly drives internalization of MOR in the cell lines we tested and underscores the utility of high-resolution cell-based assays for assessment of compound efficacy.

SIGNIFICANCE STATEMENT

G protein–coupled receptor kinases (GRKs) are attractive targets for developing therapeutics for heart failure. We have synthesized a new GRK2 subfamily–selective inhibitor, **CCG258747**, which has nanomolar potency against GRK2 and excellent selectivity over other kinases. A live-cell receptor internalization assay was used to test the ability of GRK2 inhibitors to impart efficacy on a GRK-dependent process in cells. Our data indicate that **CCG258747** blocked the internalization of the μ-opioid receptor most efficaciously because it has the ability to cross cell membranes.

Introduction

G protein–coupled receptor (GPCR) kinases (GRKs) selectively phosphorylate activated GPCRs, thereby initiating receptor endocytosis and recycling events mediated by arrestins (Ferguson et al., 1996; Gurevich et al., 2012; Gurevich and Gurevich, 2019). By terminating agonist-induced signaling, GRKs prevent prolonged activation of effector proteins and cellular stress, with the consequence of reducing receptor number at the cell surface (Rajagopal and Shenoy, 2018).

GRK-dependent regulation of activatable receptor populations has important physiologic and pathologic implications. The progression of heart failure is characterized by increased expression of GRK2 and GRK5, which are representatives of the two major GRK subfamilies, in cardiomyocytes and the concomitant reduction of β_1-adrenergic receptor (AR) density on the cell membrane (Rockman et al., 1998; Dzimiri et al., 2004; Salazar et al., 2007; Huang et al., 2011). GRK2 has also been shown to mediate desensitization of the μ-opioid receptor (MOR), an important target for analgesia, and GRK2 and GRK5 have been shown to play roles in the development of tolerance

ABBREVIATIONS: AR, adrenergic receptor; DAMGO, [D-Ala[2], N-Me-Phe[4], Gly-ol]-enkephalin; GPCR, G protein–coupled receptor; GRK, GPCR kinase; HEK, human embryonic kidney; LC-MS/MS, liquid chromatography with tandem mass spectrometry; MLM, mouse liver microsome; MOR, μ-opioid receptor; OPRM1, opioid receptor μ 1; PDB, Protein Data Bank; PKA, protein kinase A; PRKD2, protein kinase D; pSer375, phosphorylated Ser375; ROCK1, Rho-associated coiled-coil–containing kinase 1; SpH, supereliptic pHluorin.

after chronic administration of the clinically relevant analgesic morphine (Fan et al., 2002; Quillinan et al., 2011; Glück et al., 2014; Mann et al., 2015). Thus, inhibition of GRK2 and GRK5 has been identified as a promising avenue for the development of new therapeutics for diseases such as heart failure, cardiac hypertrophy, and opioid addiction (Woodall et al., 2014, 2016; Mann et al., 2015; Quillinan et al., 2011).

Our laboratory previously conducted several screens to discover GRK2-selective inhibitors (Thal et al., 2012; Homan et al., 2015), revealing that both paroxetine and **GSK180736A**, a ROCK inhibitor, could selectively inhibit GRK2 subfamily members with low micromolar or high nanomolar potency, respectively. Later, a structure-based drug design approach was used to develop derivates based on the paroxetine and **GSK180736A** scaffolds with various extensions ("D-rings") (Fig. 1) (Waldschmidt et al., 2016, 2017). Additionally, we have discovered several compounds that potently inhibit both GRK2 and GRK5 (Bouley et al., 2017; Waldschmidt et al., 2018). Development of highly potent and selective GRK5 inhibitors remains a long-term goal.

Herein, we report a new GRK2 inhibitor, **CCG258747**, our most potent GRK2 inhibitor to date that retains good selectivity over GRK5, and describe its cocrystal structure with the GRK2-G$\beta\gamma$ complex at 2.4-Å resolution. We show that this compound, along with another closely related inhibitor, **CCG258208** (Waldschmidt et al., 2017), exhibit excellent selectivity over >100 other protein kinases. To evaluate our compounds in a cellular setting that would take into account their membrane permeability, we developed an assay to monitor how our compounds affect the internalization of the MOR. We showed that **CCG258747** and **CCG258208** are both able to effectively block the internalization of MOR in two cell lines, human embryonic kidney (HEK) 293 and U2OS, which express different levels of GRKs. These effects are not mediated through inhibition of MOR phosphorylation at Ser375, as validated by western blots, suggesting a mechanism at other sites of MOR phosphorylation. Furthermore, we confirmed that efficacy in this cell-based assay is strongly linked to cell permeability, a quality that will prove useful in selecting compounds for in vivo testing. In fact, poor permeability is a liability of most compounds based on the **GSK180736A** scaffold. The fact that GRK2-selective

Fig. 1. Structures of GRK inhibitor scaffolds. Rings are labeled according to the binding mode in the GRK2 active site. The A-ring binds in the adenine subsite and interacts with the hinge, the B-ring binds in the ribose subsite, and the C-ring packs under the P-loop in the "polyphosphate subsite." The D-ring (not shown) referred to in the text is an *ortho*-substituent on the phenyl ring relative to the fluorine substituent (see Supplemental Fig. 1).

compounds performed better or as well as pan-GRK inhibitors is consistent with GRK2 being the primary GRK responsible for MOR desensitization in living cells.
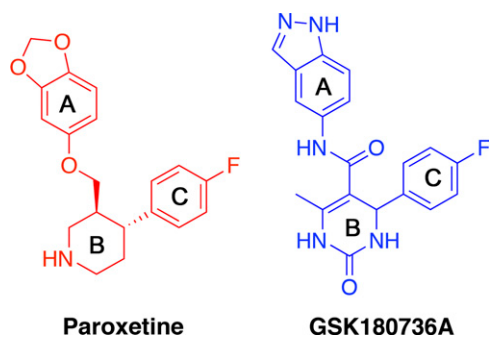
Materials and Methods

Synthesis. Synthetic procedures for **CCG258747** are provided in the supplemental data. ^{1}H NMR spectra were taken in methanol-d$_4$ at room temperature on a Varian Inova 400 MHz instrument. Reported chemical shifts for the ^{1}H NMR spectra were recorded in parts per million on the δ scale from an internal standard of residual tetramethylsilane (0 ppm). Mass spectrometry data were measured using a Waters Corporation Micromass LCT or Agilent6230 Q-TOF. High-performance liquid chromatography was used to determine purity of the compound on an Agilent 1100 series with an Agilent Zorbax Eclipse Plus−C18 column. A gradient of 10%–90% acetonitrile/water over 6 minutes followed by 90% acetonitrile/water for 7 minutes was used with detection at 254 nm. Purity of the final product was determined to be 98%.

Kinase Activity Assays. Protein kinase A (PKA) and ROCK1 inhibition were assayed using the ADP-Glo Kinase Assay system (Promega, Madison, WI) as previously described (Homan et al., 2015). Compounds were tested against PKA in duplicate using an eight-point concentration range, and the experiment was repeated in triplicate on separate days. Compounds were screened at 10 μM for ROCK1 inhibition in triplicate, the experiment repeated on three separate days, and the percent inhibition was calculated. A BMG Labtech PHERAstar imaging system was used to measure luminescence. Inhibition of GRK1, GRK2, and GRK5 was determined in 20 mM HEPES (pH 7.0), 2 mM MgCl$_2$, and 0.025% n-dodecyl β-D-maltoside with 50 nM of the respective GRK and 500 nM tubulin. Kinetic reactions were initiated by the addition of [γ-^{32}P]ATP (500 μCi, 5 μM), allowed to proceed for 8 minutes, and quenched by the addition of SDS-loading buffer. Each compound was tested in duplicate using an eight-point concentration range, and the experiment repeated on three separate days. Samples were then separated by SDS-PAGE, and gels were dried and exposed with a phosphorimaging screen. The images were then scanned with a Typhoon imager and quantified using ImageQuant, as previously described (Thal et al., 2012). Data were fit to a three-parameter dose-inhibitor response curve with a fixed Hill slope of 1 and the bottom constrained to 0 using GraphPad Prism. A maximum of two outliers were removed per individual data set using the automatic outlier rejection function, and in some cases an entire data set was excluded from the analysis.

Evaluation of Kinome Selectivity. CCG258208 and CCG258747 were tested against 104 human kinases at 1 μM using the scanELECT kinase selectivity and profiling assay panel, which was performed by the KINOMEscan division of Eurofins DiscoverX (San Diego, CA) (Fabian et al., 2005). GRK1, GRK2, GRK3, GRK4, GRK7, protein kinase D (PRKD2), and ROCK1 were added to the screen because they were not included in the standard scanELECT kinase assay panel. ROCK1 was chosen because the **GSK180736A** scaffold was originally designed as a ROCK1 inhibitor, whereas PRKD2 was chosen to provide an additional example of an AGC kinase, a kinase family in which we expected most of our off-target activity to occur.

Mouse Liver Microsome Assays. Metabolic stability was determined using CD-1 mouse liver microsomes. Reactions consisted of 1 μM compound, 0.5 mg/ml microsomes, and 1.7 mM NADPH in 0.1 M phosphate buffer (pH 7.4) supplemented with 3.3 mM MgCl$_2$ and incubated at 37°C. Aliquots of 40 μl were taken at 0, 5, 10, 15, 30, 45, and 60 minutes and quenched in three volumes of cold acetonitrile containing 100 ng/ml internal standard. Samples were centrifuged at 15,000 rpm for 10 minutes, and the supernatant was analyzed by LC-MS/MS.

Mouse Pharmacokinetic Studies. All animal experiments were approved and conducted in accordance with standards set by the University of Michigan Committee on Use and Care of Animals and

Unit for Laboratory Animal Medicine. Preliminary pharmacokinetics of **CCG258748** were determined in female CD-1 mice after intraperitoneal injection at 10 mg/kg. The compound was dissolved in 20% (v/v) DMSO, 50% (v/v) polyethylene glycol-400, and 30% (v/v) PBS. Blood samples of 50 μl were collected at 0.5, 2, 4, and 7 hours and centrifuged at 3500 rpm for 10 minutes, and the plasma were frozen at $-80°C$ for later analysis. Plasma compound concentrations were quantified using LC-MS/MS. The LC-MS/MS method consisted of a Shimadzu high-performance liquid chromatography system with a Waters Xbridge-C18 column (5 cm $\times$ 2.1 mm, 3.5 μm) for chromatographic separation of the compound. An AB Sciex QTrap 4500 mass spectrometer equipped with an electrospray ionization source (ABI-Sciex, Toronto, Canada) in the positive-ion multiple reaction–monitoring mode for detection. All pharmacokinetic parameters were calculated by noncompartmental methods using WinNonLin software, version 3.2 (Pharsight Corporation, Mountain View, CA).

Protein Expression and Purification. Human GRK2 S670A with a C-terminal hexahistidine tag was expressed in High-Five cells using the Bac-to-Bac insect cell expression system (Life Technologies, Carlsbad, CA). Cells were harvested 48 hours postinfection and lysed. GRK2 was purified from the clarified lysate as described previously for GRK1 using nickel-nitrilotriacetic acid affinity and cation-exchange chromatography (Singh et al., 2008). Fractions containing GRK2 were pooled and further purified on a Sephadex 200 column into 20 mM HEPES (pH 7.5), 100 mM NaCl, and 1 mM dithiothreitol. Soluble human $G\beta_1\gamma_2$ (C68S mutant) containing an N-terminal hexahistidine tag on the $G\beta_1$ unit was expressed using a dual-promoter insect cell expression vector in High-Five cells. The cells were harvested 48 hours postinfection and lysed. $G\beta_1\gamma_2$ was purified from the clarified lysate as described previously using nickel-nitrilotriacetic acid affinity and anion-exchange chromatography (Kozasa, 2004). Fractions containing $G\beta_1\gamma_2$ were pooled and further purified on a Sephadex 200 column into 20 mM HEPES (pH 8.0), 100 mM NaCl, and 1 mM dithiothreitol.

Crystal Structure Determination. Purified GRK2 (S670A) and soluble $G\beta_1\gamma_2$ (C68S) were mixed in a 1:1.2-M ratio with a final protein concentration of approximately 10 mg/ml. **CCG258747** (500 μM) and MgCl$_2$ (2 mM) were added to the protein mixture and allowed to incubate on ice for 30 minutes prior to filtration through a 0.2-μm Nanosep centrifugal device (Pall Laboratory, Port Washington, NY). The inhibitor complex was crystallized as previously described by hanging drop vapor diffusion at 4°C with drops consisting of 0.8 μl protein and 0.8 μl reservoir solution, which consisted of 50 mM 4-morpholineethanesulfonic acid (pH 6.0), 1.1 M NaCl, and 6% polyethylene glycol-3350 (Thal et al., 2011, 2012). Crystals generally appeared after 2 to 3 days and grew for 1 to 2 weeks. Crystals were harvested in a cryoprotectant solution consisting of the reservoir solution supplemented with 25% ethylene glycol and 500 μM inhibitor before being flash frozen in liquid nitrogen. Diffraction data were collected on the Life Sciences Collaborative Access Team beamline 21-ID-D at a wavelength of 1.0332 Å. Data integration and scaling were performed with Diffraction Integration for Advanced Light Sources (Gildea et al., 2014). The structures were solved using Phaser (McCoy et al., 2007) with Protein Data Bank (PDB) ID 4PNK as the search model. Reciprocal-space refinement was performed with PHENIX (Afonine et al., 2012) and alternated with local real-space refinement and model building using Coot (Emsley and Cowtan, 2004). Crystallographic data collection and refinement statistics are listed in Supplemental Table 1. The final model was validated using MolProbity (Chen et al., 2010) prior to deposition in the PDB under accession code 6U7C.

Cell Culture and DNA Constructs. Superecliptic pHluorin (SpH)-MOR and MOR N-terminally tagged with the pH-sensitive GFP SpH (Sankaranarayanan et al., 2000) were generated as previously described (Soohoo and Puthenveedu 2013). Stable cell lines expressing this construct were generated using HEK293 cells (CRL-1573) and U2OS cells (HTB-96) obtained from American Type Culture Collection cultured in 400 μg/ml G418 (Thermo

Fisher Scientific, Waltham, MA) (Soohoo and Puthenveedu, 2013). Once stable expression was obtained, cells were cultured in either Dulbecco's Modified Essential Medium High Glucose for HEK293 (Hyclone, Logan, UT) or McCoy's 5A Modified Medium for U2OS (Gibco, Gaithersbug, MD) supplemented with 10% FBS (Gibco) without antibiotic.

Receptor Internalization Assays. HEK293 or U2OS cells stably expressing SpH-MOR were plated at high density on 25-mm #1.5 coverslips (Electron Microscopy Sciences, Hatfield, PA) and allowed to grow to confluency for 2–4 days. Confluent coverslips were pretreated with DMSO or GRK inhibitor for 15 minutes before being transferred to a live imaging chamber where they were immersed in Leibovitz CO$_2$-independent media with 1% FBS (Gibco) containing additional DMSO or inhibitor. Fluorescence was collected using a CSU-X1 spinning disk confocal unit (Yokogawa, Sugar Land, TX), a 20 $\times$ 0.75NA objective on a Ti-E inverted microscope (Nikon Instruments, Melville, NY), excitation with a 488-nm laser line (Andor, Belfast, Ireland), a 525/30 emission filter (Semrock, Rochester, NY), and an iXon 897 EMCCD camera (Andor). The microscope stage enclosure was kept at 37°C. Twenty fields per coverslip were selected, and a baseline fluorescence was collected over four frames at 30-second intervals in each field. After baseline, cells were treated with buffer for no-treatment control or [D-Ala^2, N-Me-Phe^4, Gly-ol]-enkephalin (DAMGO) (Sigma Aldrich, St. Louis, MO) at a final concentration of 10 μM, and images were collected every 30 seconds for an additional 10 minutes. Images were analyzed using Fiji (Schindelin et al., 2012). Images were thresholded to only include pixels with intensity above 200 counts (absorbance units), which was just above the camera background of 120 counts. Receptor internalization was subsequently calculated as F_n/F_B, in which F_n is the thresholded integrated fluorescence intensity of the frame at timepoint n, and F_B is the thresholded and averaged integrated fluorescence intensity of the first four recorded frames before DAMGO addition. These calculations were automated using an open source ImageJ script (Weinberg, 2019).

Cell Permeability Determination. Compounds were submitted to Pion Inc. (Billerica, MA) for cell permeability determination using the Double-Sink parallel artificial membrane permeation assay system (Kansy et al., 1998; Avdeef, 2001). Propranolol and atenolol were used as positive and negative controls, respectively.
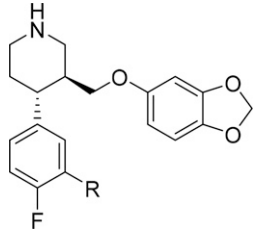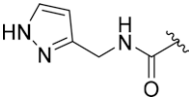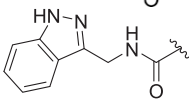
Western Blot Analysis. HEK293 or U2OS cells stably expressing SpH-MOR were plated in growth medium (Dulbecco's modified Eagle's medium + 10% FBS) at a density of 300,000 cells/well in a 12-well plate and allowed to grow to full confluency (2 to 3 days). Cells were treated with DMSO or inhibitor at 20 μM for 20 minutes, which was followed by 30 minutes of 10 μM DAMGO treatment. Cells were then lysed on ice in isotonic lysis buffer [2% SDS, 60 mM Tris (pH 6.8), Pierce Protease and Phosphatase inhibitors] and sonicated. Protein concentration was quantified using Pierce bicinchoninic acid protein estimation. Equal amounts of lysate from each condition were loaded on a 7.5% SDS-PAGE gel, and after separation they were transferred overnight to a nitrocellulose membrane. Membranes were blocked in Tris-buffered saline/Tween 20 with 5% bovine serum albumin for 1 hour and then incubated with 1:1000 anti-pSer375 OPRM1 antibody (PA5-17698; Thermo Fisher) overnight at 4°C. Membranes were developed using horseradish peroxidase–conjugated secondary antibodies (Biorad) and SuperSignal Femto ECL substrate (Thermo) and imaged using an iBright CL1000 Imaging System (Thermo). Membranes were stripped for 30 minutes at room temperature using Restore stripping buffer (Thermo) and subsequently reblocked for 1 hour in Tris-buffered saline/Tween 20 with 5% powdered milk. Membranes were incubated with 1:2000 anti-OPRM1 antibody (ab134054; Abcam) overnight, and development was repeated as above. Displayed blot is representative of two biologic replicates. Band densitometry was calculated for phospho-MOR and total MOR bands using iBright Analysis Software (Thermo). Phospho-MOR was normalized to total MOR for each sample, and then all samples were normalized to their paired DMSO treatment control

condition. Differences were evaluated using a one-way repeated measures ANOVA (GraphPad Prism).

Results

Kinase Activity Assays. Our previously reported **CCG258208** paroxetine analog with a pyrazole as its D-ring substituent had an IC$_{50}$ of 30 nM for GRK2 with 240-fold selectivity over GRK5 (Waldschmidt et al., 2017). The indazole analog **CCG258747** reported here exhibited a further increase in GRK2 potency (IC$_{50}$ = 18 nM) while retaining 83-fold selectivity over GRK5 (Supplemental Fig. 1). Additionally, **CCG258747** was more selective against GRK1 and PKA and showed little inhibition against ROCK1 at 10-μM concentration (Table 1).

Evaluation of Kinome Selectivity. Off-target activity can lead to undesired side effects because kinases play key roles in many cellular processes (Fabian et al., 2005; Yang et al., 2010; Davis et al., 2011). To more broadly assess the kinome-wide selectivity of our lead GRK2-selective paroxetine derivatives, we submitted **CCG258208** or **CCG258747** for evaluation at 1 μM in the scanELECT screen (DiscoverX) consisting of a panel of 104 kinases with the addition of GRK1, GRK2, GRK3, GRK4, GRK7, PRKD2, and ROCK1 (Fig. 2). The assay evaluated thermodynamic inhibitor-binding affinity and reports a remaining percent control activity. Compounds are assigned a selectivity score, S(35), which is a ratio of the number of hits exhibiting less than 35% of the activity of control over the number of assays performed. The S(35) selectivity scores for **CCG258208** and **CCG258747** were both 0.02, indicating that they are highly selective inhibitors. For **CCG258208** and **CCG258747** the percent control activities for GRK2 and GRK3 were 0.7% and 0.0% and 2.5% and 2.1%, respectively. The next highest activity for both compounds was against ROCK1 (50% and 47%, respectively). Only five other kinases with a percent of control activity ≤70% were observed for **CCG258747**, and

13 were observed for **CCG258208** (Supplemental Table 2). Thus, although **CCG258747** had relatively higher off-target potency against GRK1 and GRK4 (each with 67% percent control), it seemed to have less overall off-target kinase activity than **CCG258208**.

Preliminary Pharmacokinetic Studies in Mice. The stability of **CCG258747** toward incubation with mouse liver microsomes (MLMs) was evaluated to guide selection of analogs with favorable pharmacokinetic properties (Table 2). As previously reported, our lead compound, paroxetine, had a $t_{1/2}$ of 24 minutes, and the pyrazole analog, **CCG258208,** had a $t_{1/2}$ of 7.0 minutes in the MLM assay (Waldschmidt et al., 2017). We had previously found that the polar carboxamide-linked motif on the paroxetine core exhibited metabolic instability. This instability may be the result of the heterocyclic nitrogens coordinating to the heme of cytochrome P450. Favorably, the bulkier indazole carboxamide **CCG258747** exhibited a substantially higher $t_{1/2}$ in MLMs of 40 minutes. Thus, the added bulk to the heterocycle may be blocking its ability to coordinate to heme relative to the pyrazole group of **CCG258208**.

Compound **CCG258747** was further evaluated in an abbreviated in vivo pharmacokinetic study in mice (Table 2). Plasma samples were collected at four different time points over 7 hours, and drug levels in plasma were quantified after intraperitoneal injection into CD-1 mice at a dose of 10 mg/kg. After 30 minutes, **CCG258747** had a concentration of 1520 nM, whereas **CCG258208** was 2710 nM at 30 minutes (Waldschmidt et al., 2017). However, **CCG258747** maintained a slightly lower curve of clearance relative to **CCG258208**. The observed area-under-the-curve (AUC) for **CCG258747** was also lower than that of **CCG258208** (4970 vs. 5970 hours·nM). As with **CCG258208**, **CCG258747** was also able to maintain total plasma drug levels after single intraperitoneal administration that exceeded the GRK2 IC$_{50}$ for at least 7 hours, making it a suitable candidate for future in vivo efficacy studies in mice.

TABLE 1
Kinase inhibitory activity of CCG258208 and CCG258747

R	Compound	GRK2 IC$_{50}$ (μM)[a]	GRK1 IC$_{50}$ (μM)[a]	GRK5 IC$_{50}$ (μM)[a]	PKA IC$_{50}$ (μM)[a]	ROCK1[b] (%)
H	Paroxetine	1.4 ± 1	>100	>100	>100	10
	258208	0.030 ± 0.001	87 ± 30	7.1 ± 0.7	>100	9
	258747	0.018 ± 0.006	9.3 ± 3	1.5 ± 0.5	>100	27

[a]All IC$_{50}$ measurements are an average of three separate experiments run in duplicate. Errors shown represent error of the mean.
[b]Percent inhibition at 10 μM inhibitor concentration. IC$_{50}$ data for paroxetine and **CCG258208** are reproduced from Waldschmidt et al. (2017) for comparison.
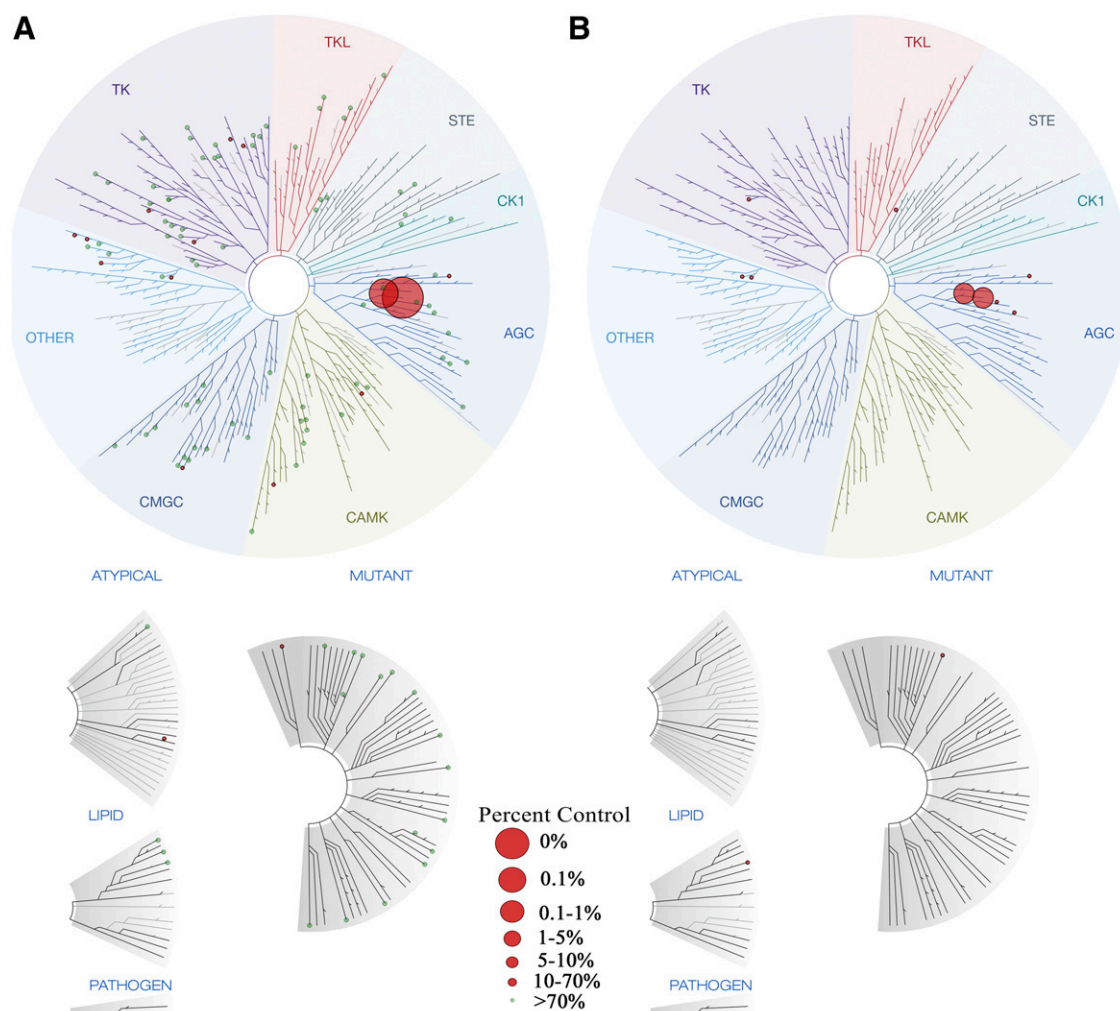
Fig. 2. Kinome selectivity of CCG258208 and CCG258747 at 1 μM. Kinome scan data for (A) CCG258208 and (B) CCG258747. Each kinase subfamily is highlighted in the kinome. Under the AGC kinase subfamily, two large red dots show the reported percent control inhibition for GRK2 and GRK3. Other kinases with a percent activity between 10% and 70% are shown as small red dots. All other kinases with a percent activity greater than 70% are represented with green dots.ACG, protein A, G, and C families; CMGC, CDK, MAPK, GSK3, and CLK families; CAMK, calmodulin/calcium regulated kinases; CK1, casein kinase 1; STE, homologs of STE7, STE11, STE20 yeast genes; TK, tyrosine kinase family; TKL, tyrosine kinase-like family.

Crystallography. The indazole analog **CCG258747** crystallized in complex with GRK2-G$\beta\gamma$ (Fig. 3A) in space group C222$_1$, a form that had not been previously observed with other paroxetine derivatives and diffracted to a resolution of 2.44 Å. This crystal form is, however, analogous to those obtained with our previously reported **GSK180736A**-derived (Waldschmidt et al., 2016, 2018) and indazole-paroxetine series compounds (Bouley et al., 2017). As with other paroxetine analogs, the benzodioxole of **CCG258747** forms hydrogen bonds with backbone atoms of Met274 and Asp272 in the kinase hinge. The central piperidine nitrogen makes a hydrogen

bond with the carbonyl of Ala321 in the ribose subsite, and the fluorophenyl group packs under the P-loop. As observed for **CCG258208** (PDB ID: 5UKM), the indazole nitrogens of **CCG258747** form hydrogen bonds with Glu239 and Lys220 in the hydrophobic subsite (Fig. 3A). The phenyl of the indazole ring packs in a manner similar to what is seen with **CCG211998** (PDB ID: 5UKK), making edge-to-face π-stacking interactions with the side chain of Phe202 at the tip of the P-loop. The indazole pushes the P-loop, αB helix, αB-αC loop, and αC helix of the kinase domain small lobe a maximum of 2.4 Å (Cα of Thr234) outward from the active

TABLE 2

In vivo exposure after intraperitoneal administration to mice

CD-1 mice were injected intraperitoneally with a single indicated dose. The data shown are mean values from three mice at each time point.

Compound (dose)	Compound Concentration in Plasma (nM)				AUC $^{obs}_{0-7\ h}$ (h·nM)
	30 min	2 h	4 h	7 h	
CCG258208 (10 mg/kg)	2710	1440	270	430	5970
CCG258747 (10 mg/kg)	1530	1150	470	170	4970

AUC, area under the curve.
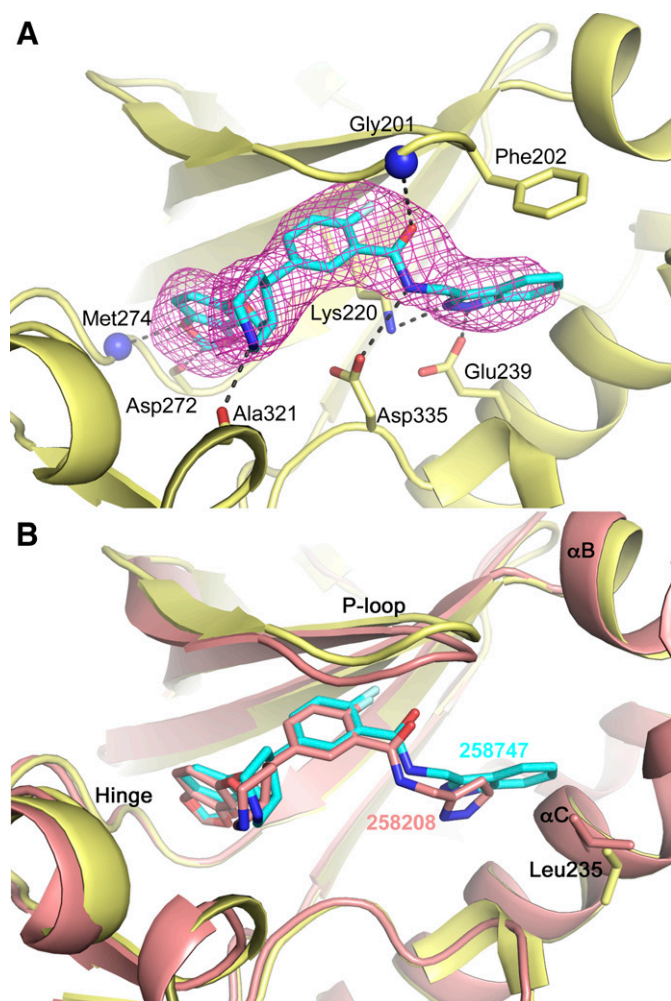
Fig. 3. Structure of GRK2-G$\beta\gamma$ in complex with CCG258747. (A) GRK2-G$\beta\gamma$·**CCG258747** crystal structure. GRK2 is in light yellow, and **CCG258747** is colored with cyan carbons. Electron density from an $|F_o|$ $-$ $|F_c|$ omit map is contoured at 3.0 σ and shown as magenta mesh. Hydrogen bonds are indicated by dashed black lines. (B) Overlay of the GRK2-G$\beta\gamma$·**CCG258208** (salmon cartoon and carbons) and GRK2-G$\beta\gamma$·**CCG258747** (light yellow cartoon and cyan carbons) atomic models.

site to form a larger pocket. The active-site tether loop, which passes over the active site, has lower temperature factors in the GRK2-G$\beta\gamma$·**CCG258747** complex compared with **CCG258208**, with residues 480–482 making direct contacts with the piperidine ring of the bound inhibitor. The overall root-mean-square deviation between the **CCG258747** and **CCG258208** complexes was 0.5 Å for all backbone atoms.

Receptor Internalization Assays. We next tested a series of our compounds including **CCG258747** and **CCG258208** (Supplemental Fig. 2) for their ability to prevent GPCR internalization using live-cell confocal microscopy, wherein we monitored the GRK-dependent internalization of an activated GPCR in real time using an SpH tag, as previously described (Vistein and Puthenveedu, 2013). Fluorescence of the SpH-tagged receptor is quenched in intracellular compartments because of their acidic pH and the pH dependence of this tag. Thus, the fluorescence intensity can be directly correlated to the total levels of receptors at the cell surface, existing at an equilibrium between receptor internalization and receptor recycling. MOR was used as a model system

because the internalization of MOR has been reported to be primarily dependent on GRK2/3 and only partially dependent on GRK5/6 (Just et al., 2013; Miess et al., 2018). Robust internalization of MOR is observed with the peptide agonist DAMGO, which leads to higher phosphorylation of Thr376 and Thr379, which are sites dependent on GRK2/3 activity (Just et al., 2013). The multisite phosphorylation patterns in MOR have also been shown to occur sequentially after initial phosphorylation of Ser375 (Just et al., 2013). Thus, we predicted that potent inhibitors of GRK2 with favorable cell permeability would significantly reduce internalization of MOR. We also predicted that inhibitors with both potency against both GRK5 and GRK2 might inhibit internalization to a greater extent given their ability to reduce phosphorylation by multiple GRK subfamilies.

Inhibitors selected for the screen featured components found in either the original paroxetine or **GSK180736A** chemical scaffolds (Supplemental Fig. 2) and were tested at 20 μM on HEK293 and U2OS cell lines stably expressing the SpH-MOR construct. Compounds were tested at 20 μM because this was the minimum concentration for CCG258747 and CCG258208 that demonstrated robust efficacy in blocking receptor internalization in HEK293 cells (Supplemental Fig. 3). Paroxetine at 50 μM was included as a control. HEK293 cells endogenously express GRK2, GRK3, GRK5, and GRK6, whereas U2OS cells express GRK2, GRK3, and GRK5 (Violin et al., 2006). Similar results were obtained for the compounds in both cell lines, with the caveat that the overall efficacy was higher in U2OS cells (Supplemental Fig. 4). **CCG258747** was the most effective at blocking MOR internalization in both cell lines, whereas **CCG258208** was the second most effective (Fig. 4). Although several of the inhibitors tested were also potent inhibitors of GRK5 ($IC_{50} < 1 \mu$M) (Table 3), they did not seem to provide any advantage in blocking the internalization of MOR in this assay in either cell line. However, the compounds with a piperidine as their B-ring (based on the paroxetine scaffold) demonstrated much better efficacy in this cell-based assay than those with a dihydropyrimidine B-ring (based on the **GSK180736A** scaffold). GRK2 potency overall seemed to drive efficacy in this assay with the notable exception of **CCG258748** (GRK2 IC_{50} = 8 nM), which showed no efficacy in HEK293 cells and only moderate efficacy in U2OS cells (Supplemental Fig. 4).

Cell Permeability Determination. We hypothesized that cell permeability was the primary reason we saw differences between compounds featuring paroxetine- or GSK-based B-rings. In order for a compound to show efficacy in blocking the internalization of MOR, they would have to cross the cell membrane and be present in the cytosol in sufficient concentrations to inhibit GRKs. Several compounds, such as **CCG224406** and **CCG215022**, did not display efficacy against MOR internalization despite being potent GRK2 inhibitors (IC_{50} values of 130 and 150 nM, respectively). We submitted eight representative compounds as well as paroxetine to Pion to determine cell permeability using the parallel artificial membrane permeation assay system (Table 3). Unsurprisingly, paroxetine demonstrated excellent membrane permeability, even outperforming the positive control propranolol. The two compounds tested with dihydropyrimidine cores (**CCG215022** and **CCG257142**) showed very poor permeability across the membrane and also poor membrane retention. Several paroxetine-based compounds showed
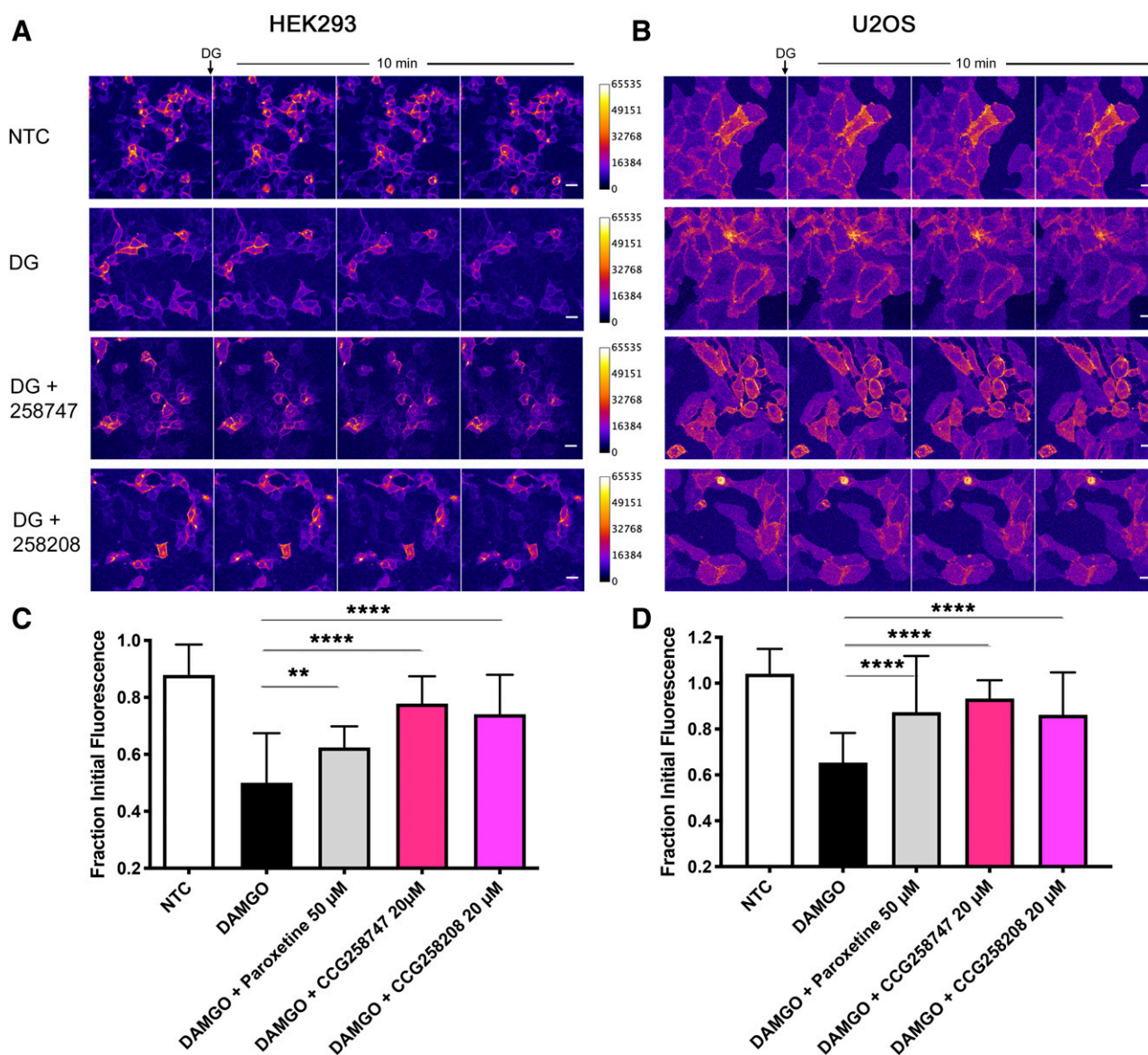
Fig. 4. Reduction of MOR internalization by CCG258747 and CCG258208. Representative images from (A) HEK293 or (B) U2OS stable cells expressing the SpH-MOR construct. NTC, no-treatment control; DG, DAMGO; DG + 258208, cells pretreated with CCG258208 and then DAMGO; DG + 258747, cells pretreated with CCG258747 and then DAMGO. Images are colored using the Fire lookup table in ImageJ. First image of each montage shows a baseline image prior to DAMGO (or buffer for NTC) addition. The following images in each montage are in 3-minute intervals with the last image showing the endpoint at 12 minutes. Scale bar, 20 μm. Quantitation was performed by normalizing the overall fluorescence to the initial signal for each experiment for (C) HEK293 and (D) U2OS cells expressing the SpH-MOR construct. Cells were pretreated with inhibitors for at least 10 minutes prior to DAMGO treatment. Endpoints are at 12 minutes and represent an average of 20 fields per coverslip (one coverslip per condition for HEK293 and three coverslips per condition for U2OS). Error bars show the S.D. Compound treatment groups were compared with DAMGO-only treatment using an unpaired t test to demonstrate statistical significance; $**P < 0.01$; $****P < 0.0001$.

significant permeability ($>1.0 \times 10^{-6}$ cm/s) and membrane retention ($>25\%$). **CCG258748** was the only paroxetine-based compound that had both poor permeability and membrane retention, which could help explain its lack of efficacy in HEK293 compared with U2OS cells. **CCG258747** had similar permeability to **CCG258208** but had greater retention in the membrane, likely due to its greater hydrophobicity. The paroxetine derivatives with the best membrane permeability were **CCG224061** and **CCG258022**, which both block lack a D-ring substituent and differ structurally from one another by only a single fluorine substituent (Supplemental Fig. 2). Additionally, **CCG224061** and **CCG258022** differ in their hinge-binding moiety (A ring), which suggests that the major

driver for solubility and permeability is the identity of the B-ring (piperidine vs. dihydropyrimidine).

Western Blot Analysis. To test how **CCG258747** and **CCG258208** affect the phosphorylation of MOR in our assay system, we blotted for MOR using an antibody selective for pSer375, which is the only commercially available phosphosite-specific antibody for MOR. Upon DAMGO treatment we observed an increase in pSer375-MOR for both HEK293 and U2OS stable cells, as expected (Fig. 5). In the presence of **CCG258747** but not **CCG258208** phosphorylation of Ser375 was reduced, although not in a statistically significant manner (Supplemental Fig. 5). This suggests the possibility that these compounds instead exert their effect on MOR internalization

TABLE 3
GRK inhibition, cell permeability, and membrane retention of key inhibitors

Values are averages of $n = 4$ at pH of 7.4. Error for P_e and %R are shown as S.D. GRK2 and GRK5 IC$_{50}$ values are reproduced here for ease of comparison and represent an average of three separate experiments run in duplicate. Corresponding references are provided for previously published data.

Compound #	Avg P_e ($\times 10^{-6}$ cm/s)	Avg %R	GRK2 IC$_{50}$ (μM)	GRK5 IC$_{50}$ (μM)	Reference for IC$_{50}$ Data
Paroxetine	92 ± 7	34 ± 2	1.4	>100	Waldschmidt et al., 2017
258748	<0.3	8 ± 1	0.008	0.24	Bouley et al., 2017
258747	1.2 ± 0.1	78 ± 1	0.018	1.5	Table 1
258208 (14as)	1.4 ± 0.7	46 ± 1	0.03	7.1	Waldschmidt et al., 2017
224061	23 ± 1	66 ± 1	0.066	1.3	Bouley et al., 2017
257284	<0.5	29 ± 2	0.10	0.50	Bouley et al., 2017
258002	18 ± 3	69 ± 3	0.14	3.7	Bouley et al., 2017
GSK180736A	ND	ND	0.77	>100	Waldschmidt et al., 2016
224406 (12n)	ND	ND	0.13	>100	Waldschmidt et al., 2016
215022 (12 h)	0.21 ± 0.05	5 ± 1	0.15	0.38	Waldschmidt et al., 2016
257142 (33)	0.12 ± 0.01	6 ± 1	0.25	0.26	Waldschmidt et al., 2018
Propanolol	79 ± 10	31 ± 2	NA	NA	
Atenolol	<0.4	8 ± 1	NA	NA	

NA, not applicable ND, not done; P_e, effective permeability; %R, percent membrane retention.

by reducing phosphorylation of other residues on the C-terminal tail of MOR, such as Thr376 and Thr379.

Discussion

Replacement of the pyrazole of **CCG258208** with an indazole to give **CCG258747** resulted in a more potent GRK2 inhibitor (IC$_{50}$ = 18 nM) with high selectivity over GRK1, GRK5, PKA, and ROCK1 (518-, 83-, >5500-, and >550-fold, respectively). The high selectivity of both inhibitors was further validated in a kinome selectivity scan wherein both **CCG258208** and **CCG258747** were able to inhibit GRK2 and GRK3 activity below 2.5% of control with very little off-target activity. Evaluation in a short pharmacokinetics study revealed that **CCG258747**, like **CCG245208**, was able to maintain plasma concentrations higher than its IC$_{50}$ for over 7 hours, which was indicative of its potential as an in vivo therapeutic.

Crystallization of **CCG258747** further shows that its indazole ring takes advantage of conformational flexibility in the hydrophobic subsite of GRK2, as evidenced by comparing the structure of GRK2-G$\beta\gamma$· **CCG258747** to that of **CCG258208**. One might hypothesize that GRK2 has more latitude to accommodate bulky substituents within its hydrophobic subsite than the other GRK subfamilies or other kinases. However, this cannot explain the exceptional selectivity of **CCG258747** for GRK2 subfamily members relative to the rest of the kinome because **CCG258208**, with the smaller pyrazole D-ring, is similarly selective. Instead, it selectively appears to be largely dictated by unique interactions of the benzodioxole ring with the GRK2 hinge, with the added van der Waals interactions with the indazole D-ring of **CCG258747** contributing to enhanced potency. Indeed, the indazole substitution enhances potency against all GRKs tested relative to CCG258208 (Table 1).

A live-cell receptor internalization assay using MOR as a model system was used to test the ability of these inhibitors to function in cells, which we hypothesized would be a better read-out of their suitability for in vivo trials than IC$_{50}$ values because it takes into account the ability of these compounds to cross the cell membrane in sufficient amounts to achieve levels at or above their GRK2 IC$_{50}$ in the cytosol. Overall, inhibitors with the piperidine B-ring of the paroxetine scaffold demonstrated much better efficacy than those based on the **GSK180736A** B-ring (Fig. 4), with **CCG258747** demonstrating the highest efficacy of the inhibitors tested. Our results are consistent with other recent studies on the ability of paroxetine to inhibit phosphorylation of the β_2-AR and reduce internalization of the β_1- and β_2-ARs in HEK293 and U2OS cells, respectively (Guo et al., 2017), thus demonstrating the utility of paroxetine analogs for inhibiting the proximal effects of GRKs in multiple cell types for multiple GPCRs. An assay for cell permeability similarly showed that paroxetine-based inhibitors in general also demonstrated
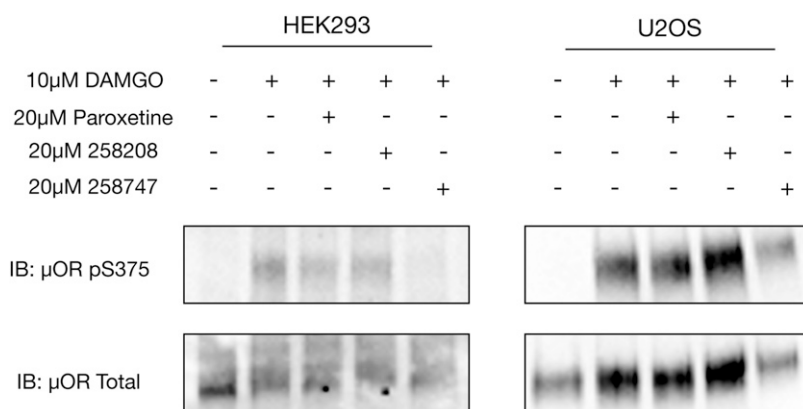
Fig. 5. Effect of GRK2 inhibitors on phosphorylation of MOR-Ser375. Cell lysates from MOR stable cell lines of either HEK293 (left) or U2OS (right) were blotted for phospho-Ser375 using an anti-pSer375-OPRM1 antibody (top blots) and blotted for total receptor (bottom blots) with an anti-OPRM1. For paroxetine, CCG258208, and CCG258747 treatments, the cells were pretreated with inhibitor for 20 minutes prior to the addition of DAMGO. IB, immunoblot.

better cell permeability properties than the **GSK180736A** scaffold (Table 3). Thus, our assay can select for compounds that combine high GRK2 potency with favorable cell permeability.

Finally, we note that GRK inhibitors with potency against both GRK2 and GRK5 (marked with plus symbols in Fig. 4) in general were unable to inhibit MOR internalization better than those with high GRK2 selectivity. Cell permeability was far more predictive of efficacy. This result is consistent with our observation that phosphorylation of MOR at Ser375 is not significantly affected by GRK2 inhibition (Fig. 5; Supplemental Fig. 5), because this site is believed to be phosphorylated primarily by GRK5 (Doll et al., 2011; Just et al., 2013), whereas higher order phosphorylation at other sites is thought to be GRK2-mediated (Mann et al., 2015). A hierarchical model of MOR phosphorylation, in which Ser375 is phosphorylated with subsequent recruitment of GRK2 to phosphorylate other sites in the MOR C-terminal tail, has been previously proposed and recently demonstrated using in-cell assays to assess MOR recruitment of GRK2 (Just et al., 2013; Miess et al., 2018). Hierarchical phosphorylation is reportedly key for rapid receptor desensitization, high-affinity arrestin binding, and long-term receptor desensitization via receptor internalization (Miess et al., 2018; Sente et al., 2018). Thus, at least in these cell systems, our data suggest that phosphorylation of MOR by GRK2 subfamily members dominates arrestin recruitment and internalization. As data continue to gather implicating MOR phosphorylation as a primary mediator of drug-specific receptor tolerance in vivo (Arttamangkul et al., 2019; Kliewer et al., 2019), the chemical probes described in this study may prove to be important tools through their potential ability to selectively alter MOR phosphorylation in vivo.

Acknowledgments

Authorship Contributions

Participated in research design: Bouley, Weinberg, Yen, Larsen, Puthenveedu, Tesmer.

Conducted experiments: Bouley, Weinberg, Waldschmidt, Yen.

Contributed new reagents or analytic tools: Waldschmidt.

Performed data analysis: Bouley, Weinberg, Waldschmidt.

Wrote or contributed to the writing of the manuscript: Bouley, Weinberg, Waldschmidt, Tesmer.

References

Afonine PV, Grosse-Kunstleve RW, Echols N, Headd JJ, Moriarty NW, Mustyakimov M, Terwilliger TC, Urzhumtsev A, Zwart PH, and Adams PD (2012) Towards automated crystallographic structure refinement with phenix.refine. *Acta Crystallogr D Biol Crystallogr* **68**:352–367.

Arttamangkul S, Leff ER, Koita O, Birdsong WT, and Williams JT (2019) Separation of acute desensitization and long-term tolerance of μ-opioid receptors is determined by the degree of C-terminal phosphorylation. *Mol Pharmacol* **96**:505–514.

Avdeef A (2001) Physicochemical profiling (solubility, permeability and charge state). *Curr Top Med Chem* **1**:277–351.

Bouley R, Waldschmidt HV, Cato MC, Cannavo A, Song J, Cheung JY, Yao X-Q, Koch WJ, Larsen SD, and Tesmer JJG (2017) Structural determinants influencing the potency and selectivity of indazole-paroxetine hybrid G protein-coupled receptor kinase 2 inhibitors. *Mol Pharmacol* **92**:707–717.

Chen VB, Arendall WB III, Headd JJ, Keedy DA, Immormino RM, Kapral GJ, Murray LW, Richardson JS, and Richardson DC (2010) MolProbity: all-atom structure validation for macromolecular crystallography. *Acta Crystallogr D Biol Crystallogr* **66**:12–21.

Davis MI, Hunt JP, Herrgard S, Ciceri P, Wodicka LM, Pallares G, Hocker M, Treiber DK, and Zarrinkar PP (2011) Comprehensive analysis of kinase inhibitor selectivity. *Nat Biotechnol* **29**:1046–1051.

Doll C, Konietzko J, Pöll F, Koch T, Höllt V, and Schulz S (2011) Agonist-selective patterns of μ-opioid receptor phosphorylation revealed by phosphosite-specific antibodies. *Br J Pharmacol* **164**:298–307.

Dzimiri N, Muiya P, Andres E, and Al-Halees Z (2004) Differential functional expression of human myocardial G protein receptor kinases in left ventricular cardiac diseases. *Eur J Pharmacol* **489**:167–177.

Emsley P and Cowtan K (2004) Coot: model-building tools for molecular graphics. *Acta Crystallogr D Biol Crystallogr* **60**:2126–2132.

Fabian MA, Biggs WH III, Treiber DK, Atteridge CE, Azimioara MD, Benedetti MG, Carter TA, Ciceri P, Edeen PT, Floyd M, et al. (2005) A small molecule-kinase interaction map for clinical kinase inhibitors. *Nat Biotechnol* **23**:329–336.

Fan X, Zhang J, Zhang X, Yue W, and Ma L (2002) Acute and chronic morphine treatments and morphine withdrawal differentially regulate GRK2 and GRK5 gene expression in rat brain. *Neuropharmacology* **43**:809–816.

Ferguson SS, Downey WE III, Colapietro AM, Barak LS, Ménard L, and Caron MG (1996) Role of beta-arrestin in mediating agonist-promoted G protein-coupled receptor internalization. *Science* **271**:363–366.

Gildea RJ, Waterman DG, Parkhurst JM, Axford D, Sutton G, Stuart DI, Sauter NK, Evans G, and Winter G (2014) New methods for indexing multi-lattice diffraction data. *Acta Crystallogr D Biol Crystallogr* **70**:2652–2666.

Glück L, Loktev A, Moulédous L, Mollereau C, Law P-Y, and Schulz S (2014) Loss of morphine reward and dependence in mice lacking G protein-coupled receptor kinase 5. *Biol Psychiatry* **76**:767–774.

Guo S, Carter RL, Grisanti LA, Koch WJ, and Tilley DG (2017) Impact of paroxetine on proximal β-adrenergic receptor signaling. *Cell Signal* **38**:127–133.

Gurevich EV, Tesmer JJG, Mushegian A, and Gurevich VV (2012) G protein-coupled receptor kinases: more than just kinases and not only for GPCRs. *Pharmacol Ther* **133**:40–69.

Gurevich VV and Gurevich EV (2019) GPCR signaling regulation: the role of GRKs and arrestins. *Front Pharmacol* **10**:125.

Homan KT, Larimore KM, Elkins JM, Szklarz M, Knapp S, and Tesmer JJG (2015) Identification and structure-function analysis of subfamily selective G protein-coupled kinase inhibitors. *ACS Chem Biol* **10**:310–319.

Huang ZM, Gold JI, and Koch WJ (2011) G protein-coupled receptor kinases in normal and failing myocardium. *Front Biosci* **16**:3047–3060.

Just S, Illing S, Trester-Zedlitz M, Lau EK, Kotowski SJ, Miess E, Mann A, Doll C, Trinidad JC, Burlingame AL, et al. (2013) Differentiation of opioid drug effects by hierarchical multi-site phosphorylation. *Mol Pharmacol* **83**:633–639.

Kansy M, Senner F, and Gubernator K (1998) Physicochemical high throughput screening: parallel artificial membrane permeation assay in the description of passive absorption processes. *J Med Chem* **41**:1007–1010.

Kliewer A, Schmiedel F, Sianati S, Bailey A, Bateman JT, Levitt ES, Williams JT, Christie MJ, and Schulz S (2019) Phosphorylation-deficient G-protein-biased μ-opioid receptors improve analgesia and diminish tolerance but worsen opioid side effects. *Nat Commun* **10**:367.

Kozasa T (2004) Purification of G protein subunits from Sf9 insect cells using hexahistidine-tagged alpha and beta gamma subunits. *Methods Mol Biol* **237**:21–38.

Mann A, Illing S, Miess E, and Schulz S (2015) Different mechanisms of homologous and heterologous μ-opioid receptor phosphorylation. *Br J Pharmacol* **172**:311–316.

McCoy AJ, Grosse-Kunstleve RW, Adams PD, Winn MD, Storoni LC, and Read RJ (2007) Phaser crystallographic software. *J Appl Cryst* **40**:658–674.

Miess E, Gondin AB, Yousuf A, Steinborn R, Mösslein N, Yang Y, Göldner M, Ruland JG, Bünemann M, Krasel C, et al. (2018) Multisite phosphorylation is required for sustained interaction with GRKs and arrestins during rapid μ-opioid receptor desensitization. *Sci Signal* **11**:eaas9609.

Quillinan N, Lau EK, Virk M, von Zastrow M, and Williams JT (2011) Recovery from mu-opioid receptor desensitization after chronic treatment with morphine and methadone. *J Neurosci* **31**:4434–4443.

Rajagopal S and Shenoy SK (2018) GPCR desensitization: acute and prolonged phases. *Cell Signal* **41**:9–16.

Rockman HA, Choi DJ, Akhter SA, Jaber M, Giros B, Lefkowitz RJ, Caron MG, and Koch WJ (1998) Control of myocardial contractile function by the level of beta-adrenergic receptor kinase 1 in gene-targeted mice. *J Biol Chem* **273**:18180–18184.

Salazar NC, Chen J, and Rockman HA (2007) Cardiac GPCRs: GPCR signaling in healthy and failing hearts. *Biochim Biophys Acta* **1768**:1006–1018.

Sankaranarayanan S, De Angelis D, Rothman JE, and Ryan TA (2000) The Use of pHluorins for Optical Measurements of Presynaptic Activity. *Biophysical Journal* **79**:2199–2208, doi: 10.1016/S0006-3495(00)76468-X 11023924.

Schindelin J, Arganda-Carreras I, Frise E, Kaynig V, Longair M, Pietzsch T, Preibisch S, Rueden C, Saalfeld S, Schmid B, et al. (2012) Fiji: an open-source platform for biological-image analysis. *Nat Methods* **9**:676–682.

Sente A, Peer R, Srivastava A, Baidya M, Lesk AM, Balaji S, Shukla AK, Babu MM, and Flock T (2018) Molecular mechanism of modulating arrestin conformation by GPCR phosphorylation. *Nat Struct Mol Biol* **25**:538–545.

Singh P, Wang B, Maeda T, Palczewski K, and Tesmer JJG (2008) Structures of rhodopsin kinase in different ligand states reveal key elements involved in G protein-coupled receptor kinase activation. *J Biol Chem* **283**:14053–14062.

Soohoo AL and Puthenveedu MA (2013) Divergent modes for cargo-mediated control of clathrin-coated pit dynamics. *Mol Biol Cell* **24**:1725–1734, doi: 10.1091/mbc.E12-07-0550 23536704.

Thal DM, Homan KT, Chen J, Wu EK, Hinkle PM, Huang ZM, Chuprun JK, Song J, Gao E, Cheung JY, et al. (2012) Paroxetine is a direct inhibitor of g protein-coupled receptor kinase 2 and increases myocardial contractility. *ACS Chem Biol* **7**:1830–1839.

Thal DM, Yeow RY, Schoenau C, Huber J, and Tesmer JJG (2011) Molecular mechanism of selectivity among G protein-coupled receptor kinase 2 inhibitors. *Mol Pharmacol* **80**:294–303.

Violin JD, Ren X-R, and Lefkowitz RJ (2006) G-protein-coupled receptor kinase specificity for beta-arrestin recruitment to the beta2-adrenergic receptor

revealed by fluorescence resonance energy transfer. *J Biol Chem* **281**: 20577–20588.

Vistein R and Puthenveedu MA (2013) Reprogramming of G protein-coupled receptor recycling and signaling by a kinase switch. *Proc Natl Acad Sci USA* **110**:15289–15294.

Waldschmidt HV, Bouley R, Kirchhoff PD, Lee P, Tesmer JJG, and Larsen SD (2018) Utilizing a structure-based docking approach to develop potent G protein-coupled receptor kinase (GRK) 2 and 5 inhibitors. *Bioorg Med Chem Lett* **28**:1507–1515.

Waldschmidt HV, Homan KT, Cato MC, Cruz-Rodríguez O, Cannavo A, Wilson MW, Song J, Cheung JY, Koch WJ, Tesmer JJ, et al. (2017) Structure-based design of highly selective and potent G protein-coupled receptor kinase 2 inhibitors based on paroxetine. *J Med Chem* **60**:3052–3069.

Waldschmidt HV, Homan KT, Cruz-Rodríguez O, Cato MC, Waninger-Saroni J, Larimore KM, Cannavo A, Song J, Cheung JY, Kirchhoff PD, et al. (2016) Structure-based design, synthesis, and biological evaluation of highly selective and potent G protein-coupled receptor kinase 2 inhibitors. *J Med Chem* **59**:3793–3807.

Weinberg Z (2019) *Ensemble-recycling*, Zenodo, doi: 10.5281/zenodo.2645754.

Woodall MC, Ciccarelli M, Woodall BP, and Koch WJ (2014) G protein-coupled receptor kinase 2: a link between myocardial contractile function and cardiac metabolism. *Circ Res* **114**:1661–1670.

Woodall MC, Woodall BP, Gao E, Yuan A, and Koch WJ (2016) Cardiac fibroblast GRK2 deletion enhances contractility and remodeling following ischemia/reperfusion injury. *Circ Res* **119**:1116–1127.

Yang X, Huang Y, Crowson M, Li J, Maitland ML, and Lussier YA (2010) Kinase inhibition-related adverse events predicted from in vitro kinome and clinical trial data. *J Biomed Inform* **43**:376–384.

Address correspondence to: John J.G. Tesmer, Departments of Biological Sciences and of Medicinal Chemistry and Molecular Pharmacology, Purdue University, 915 W. State St., HOCK 329, West Lafayette, IN 47907. E-mail: jtesmer@purdue.edu

A New Paroxetine-Based GRK2 Inhibitor Abrogates the Internalization of the

μ-Opioid Receptor

Renee A Bouley, Zara Y Weinberg, Helen V Waldschmidt, Yu-Chen Yen, Scott D Larsen,

Manojkumar A Puthenveedu, John J G Tesmer

Life Sciences Institute (R.A.B. and H.V.W), Department of Medicinal Chemistry (H.V.W. and

S.D.L), Department of Pharmacology (R.A.B., Z.Y.W., and M.A.P.), Vahlteich Medicinal

Chemistry Core, College of Pharmacy (H.V.W and S.D.L.), University of Michigan, Ann Arbor,

Michigan. Departments of Biological Sciences and of Medicinal Chemistry and Molecular

Pharmacology (Y-C.Y., J.J.G.T), Purdue University, West Lafayette, Indiana.

Supplementary Information

Supplementary Methods.

Synthesis of CCG258747.

tert-butyl (3S,4R)-4-(3-(((1H-indazol-3-yl)methyl)carbamoyl)-4-fluorophenyl)-3-((benzo[d][1,3]dioxol-5-yloxy)methyl)piperidine-1-carboxylate (2). 5-((3S,4R)-3-((benzo[d][1,3]dioxol-5-yloxy)methyl)-1-(*tert*-butoxycarbonyl)piperidin-4-yl)-2-fluorobenzoic acid **1** (0.08 g, 0.169 mmol), 1-ethyl-3-(3-dimethylaminopropyl)carbodiimide (0.073 g, 0.338 mmol), *N,N*-diisopropylethylamine (0.131 mL, 0.676 mmol), hydroxybenzotriazole (0.051g, 0.338 mmol), and 3H – (aminomethyl) – 1H – indazole (0.050 g, 0.338 mmol) were added to THF (5 mL) in a 15 mL round bottom flask and stirred overnight at room temperature. The resulting solution was diluted with ethyl acetate and saturated sodium bicarbonate, and then the layers were separated. The organic layer was then washed with brine (2x), dried with MgSO4, and concentrated *in vacuo*. The crude product was purified using flash chromatography using an isocratic gradient of 40% EtOAc/Hexanes to give the desired product as a white solid (83 mg, 82% yield). ^{1}H NMR (400 MHz, Methanol-d_4) δ 7.97 (s, 1H), 7.85 (d, J = 8.2 Hz, 1H), 7.60 (d, J = 6.9 Hz, 1H), 7.48 (d, J = 8.4 Hz, 1H), 7.37 (t, J = 7.8 Hz, 2H), 7.11 (t, J = 7.7 Hz, 2H), 6.57 (d, J = 8.5 Hz, 1H), 6.33 (d, J = 2.2 Hz, 1H), 6.13 (dd, J = 8.9, 2.4 Hz, 1H), 5.82 (s, 2H), 4.94 (s, 2H), 4.40 (d, J = 13.0 Hz, 1H), 4.18 (d, J = 13.6 Hz, 1H), 3.57 (d, J = 9.4 Hz, 1H), 3.49 (t, J = 8.6 Hz, 1H), 2.88 (s, 1H), 2.82 – 2.71 (m, 2H), 2.05 (s, 1H), 1.76 (s, 1H), 1.75 – 1.61 (m, 1H), 1.48 (s, 9H). HPLC purity: 98%.

*N-((1H-indazol-3-yl)methyl)-5-((3S,4R)-3-((benzo[d][1,3]dioxol-5-yloxy)methyl)piperidin-4-yl)-2-fluorobenzamide (**3**)*. tert-butyl (3S,4R)-4-(3-(((1H-indazol-3-yl)methyl)carbamoyl)-4-fluorophenyl)-3-((benzo[d][1,3]dioxol-5-yloxy)methyl)piperidine-1-carboxylate (**2**) (0.07 g,

0.144 mmol) was dissolved in 1,4-dioxanes (2 mL) followed by 4M HCl/1,4-dioxanes (2 mL) and stirred at room temperature for two hours. The reaction was concentrated *in vacuo*, then purified using 10% MeOH/DCM to give an amorphous solid (44 mg, 51% yield). ^{1}H NMR (400 MHz, Methanol-d_4) δ 7.85 (dd, J = 8.2, 1.1 Hz, 1H), 7.61 (dd, J = 6.9, 2.3 Hz, 1H), 7.48 (dd, J = 8.5, 1.0 Hz, 1H), 7.36 (tq, J = 6.8, 1.8, 1.0 Hz, 2H), 7.14 – 7.04 (m, 2H), 6.54 (d, J = 8.5 Hz, 1H), 6.30 (d, J = 2.5 Hz, 1H), 6.09 (dd, J = 8.5, 2.5 Hz, 1H), 5.86 – 5.77 (m, 2H), 4.93 (s, 2H), 3.52 (dd, J = 9.7, 3.0 Hz, 1H), 3.44 (dd, J = 9.7, 6.7 Hz, 1H), 3.34 – 3.26 (m, 1H), 3.14 – 3.05 (m, 1H), 2.76 – 2.58 (m, 3H), 2.08 (dtd, J = 10.8, 7.3, 6.7, 3.1 Hz, 1H), 1.78 – 1.63 (m, 2H). MS (ESI+) *m/z*: 503.2 (M+1). HPLC purity: 98%.

Supplementary Results.

Supplementary Table 1. Crystallographic Data and Refinement Statistics for GRK2-Gβγ·CCG258747 Complex.

	CCG258747
X-ray source	APS 21-ID-D
Wavelength (Å)	1.0332
D_{min} (Å)	57.9-2.44
	(2.53-2.44)
Space group	$C222_1$
Cell constants (Å)	$a = 60.6$
	$b = 240.6$
	$c = 214.6$
Unique reflections	58983 (5845)
Multiplicity	13.5 (13.7)
R_{merge} (%)	24.3 (403)
R_{pim} (%)	6.8 (112.3)
Completeness (%)	99.22 (95.66)
$<I>/<\sigma_I>$	7.25 (0.66)
$CC_{1/2}$	0.997 (0.644)
Refinement resolution	57.9-2.44
	(2.47-2.44)
Total reflections used	58564 (5595)
Protein atoms	8184
Ligand atoms	37
Water molecules	121
RMSD bonds (Å)	0.004
RMSD angles (°)	0.97
Ramachandran plot	
Favored, outliers (%)	96, 0.2
Average B-factor (Å^2)	91.29
Protein	91.82
Ligand	76.76
Solvent	60.36
R_{work}	0.243
R_{free}	0.273
PDB ID	

Supplementary Table 2. Kinome Selectivity Data for CCG258208 and CCG25747

DiscoverX Gene Symbol	% Control Activity 1 µM of 258208	% Control Activity 1 µM of 258747
ABL1(E255K)-phosphorylated	97	100
ABL1(T315I)-phosphorylated	72	97
ABL1-nonphosphorylated	91	87
ABL1-phosphorylated	94	49
ACVR1B	76	100
ADCK3	100	85
AKT1	100	80
AKT2	100	97
ALK	61	100
AURKA	82	100
AURKB	77	91
AXL	91	86
BMPR2	89	100
BRAF	76	100
BRAF(V600E)	82	100
BTK	97	100
CDK11	100	98
CDK2	100	91
CDK3	88	100
CDK7	100	98
CDK9	100	89
CHEK1	100	100
CSF1R	98	92
CSNK1D	87	87
CSNK1G2	100	100
DCAMKL1	73	79
DYRK1B	100	86
EGFR	78	96
EGFR(L858R)	100	100
EPHA2	100	100
ERBB2	100	100
ERBB4	97	100
ERK1	100	100
FAK	100	100
FGFR2	100	85
FGFR3	100	83
FLT3	95	95
GRK1	81	67
GRK2	0.7	2.5
GRK3	0	2.1

DiscoverX Gene Symbol	% Control Activity 1 μM of 258208	% Control Activity 1 μM of 258747
GRK4	99	67
GRK7	100	97
GSK3B	93	84
IGF1R	97	84
IKK-alpha	68	58
IKK-beta	81	58
INSR	100	100
JAK2(JH1domain-catalytic)	93	100
JAK3(JH1domain-catalytic)	77	100
JNK1	83	81
JNK2	75	73
JNK3	67	91
KIT	82	99
KIT(D816V)	100	88
KIT(V559D,T670I)	74	100
LKB1	100	99
MAP3K4	94	92
MAPKAPK2	100	100
MARK3	86	98
MEK1	77	94
MEK2	82	92
MET	100	100
MKNK1	87	100
MKNK2	62	100
MLK1	100	100
p38-alpha	100	100
p38-beta	95	100
PAK1	99	76
PAK2	93	70
PAK4	97	100
PCTK1	75	100
PDGFRA	52	91
PDGFRB	74	79
PDPK1	100	80
PIK3C2B	85	56
PIK3CA	100	97
PIK3CG	79	100
PIM1	100	90
PIM2	100	100
PIM3	100	87
PKAC-alpha	100	84
PLK1	55	100
PLK3	64	100
PLK4	84	95

| DiscoverX Gene Symbol	% Control Activity 1 µM of 258208	% Control Activity 1 µM of 258747
PRKCE	99	99
PRKD2	89	90
RAF1	100	100
RET	88	96
RIOK2	52	71
ROCK1	50	47
ROCK2	81	85
RSK2(Kin.Dom.1-N-terminal)	84	100
SNARK	64	95
SRC	100	94
SRPK3	96	99
TGFBR1	100	100
TIE2	100	100
TRKA	63	88
TSSK1B	100	76
TYK2(JH1domain-catalytic)	100	100
ULK2	70	100
VEGFR2	65	84
YANK3	98	91
ZAP70	86	100

*Percent control activities below 70% are highlighted in gray.
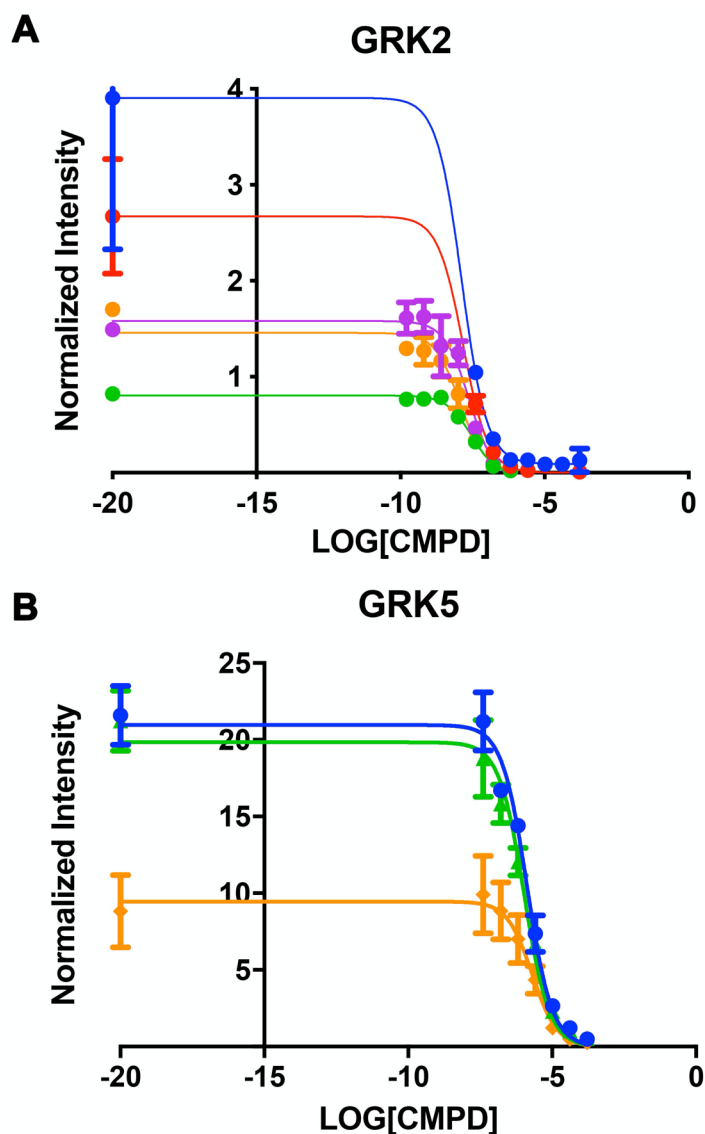
Supplementary Figure 1. CCG258747 Inhibition of GRK2 and GRK5. The phosphorylation of tubulin was monitored using ^{32}P-labeled ATP in the presence of varying concentrations of CCG258747. Band intensity was plotted versus log[CCG258747] for (A) GRK2 and (B) GRK5. Data was fit to a three-parameter dose-inhibitor response curve with a fixed Hill slope of 1 and the bottom constrained to 0 using GraphPad Prism. IC$_{50}$'s from at least 3 experiments performed in duplicate were then averaged.
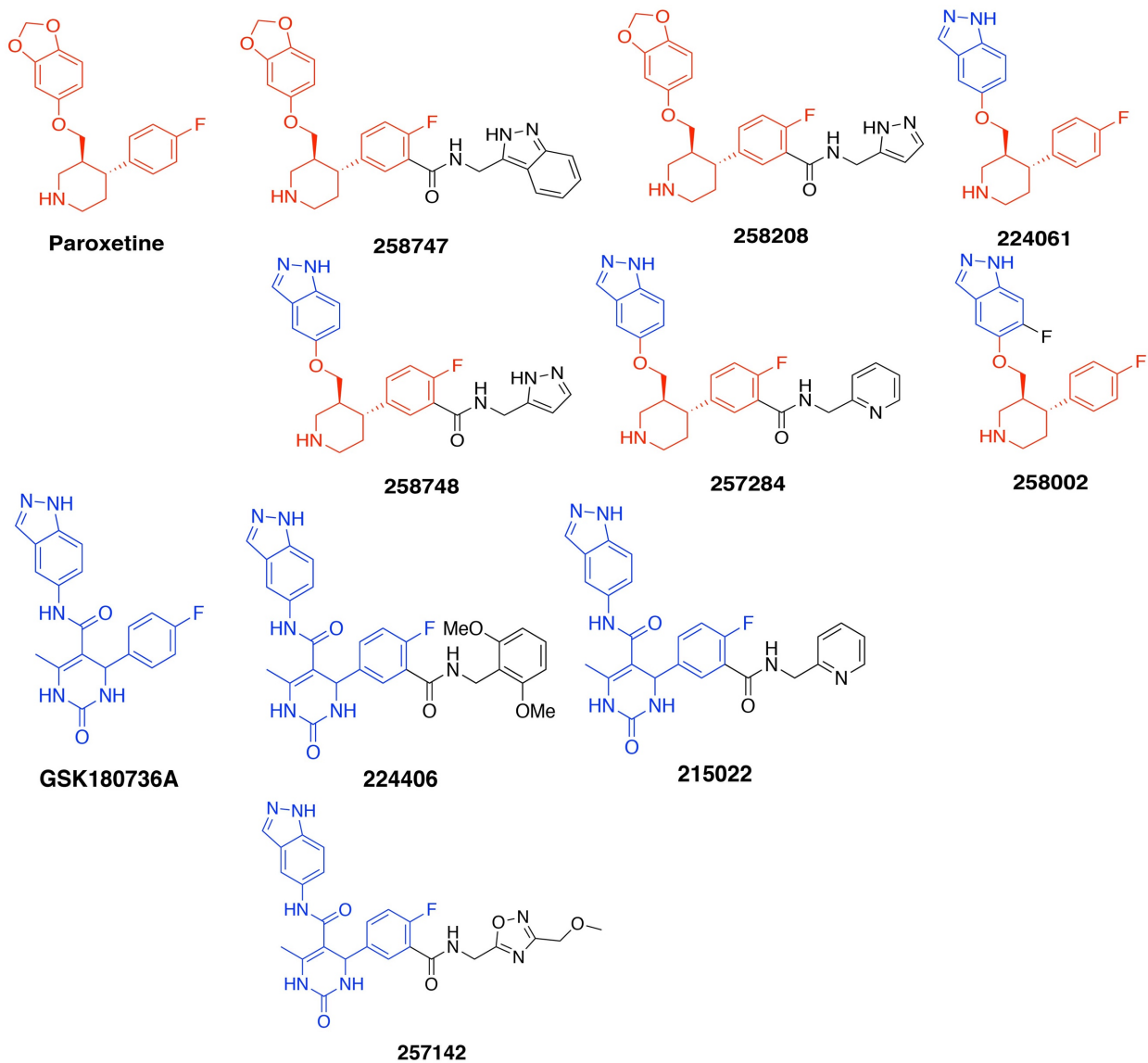
Supplemental Figure 2. Chemical structures of compounds evaluated for efficacy in the receptor internalization assay. Scaffolds and substituents based on **GSK180736A** are colored blue and those based on paroxetine are colored red. D-ring substituents are colored in black.
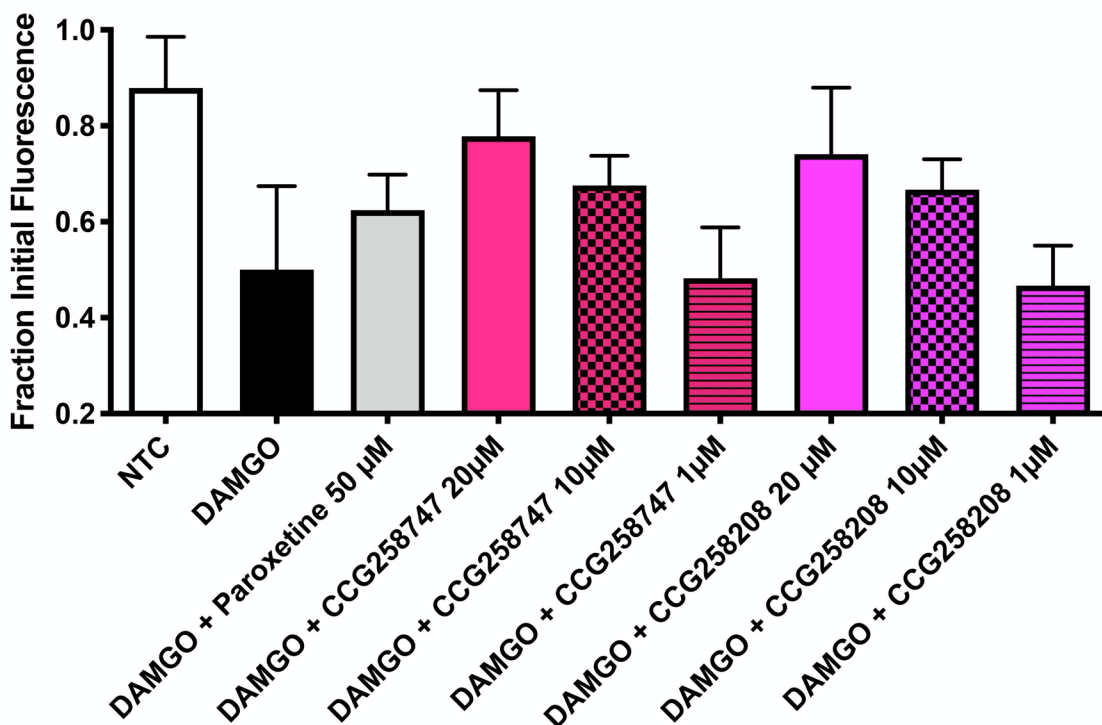
Supplementary Figure 3. MOR Internalization Dose Response of 258747 and 258208.
Quantitation was performed by normalizing the overall fluorescence to the initial signal for each experiment for HEK293 expressing the SpH-MOR construct. Cells were pre-treated with inhibitors for at least 10 min prior to DAMGO treatment. Endpoints are at 12 min and represent an average of 20 fields per coverslip (1 coverslip per condition). Error bars show the standard deviation.
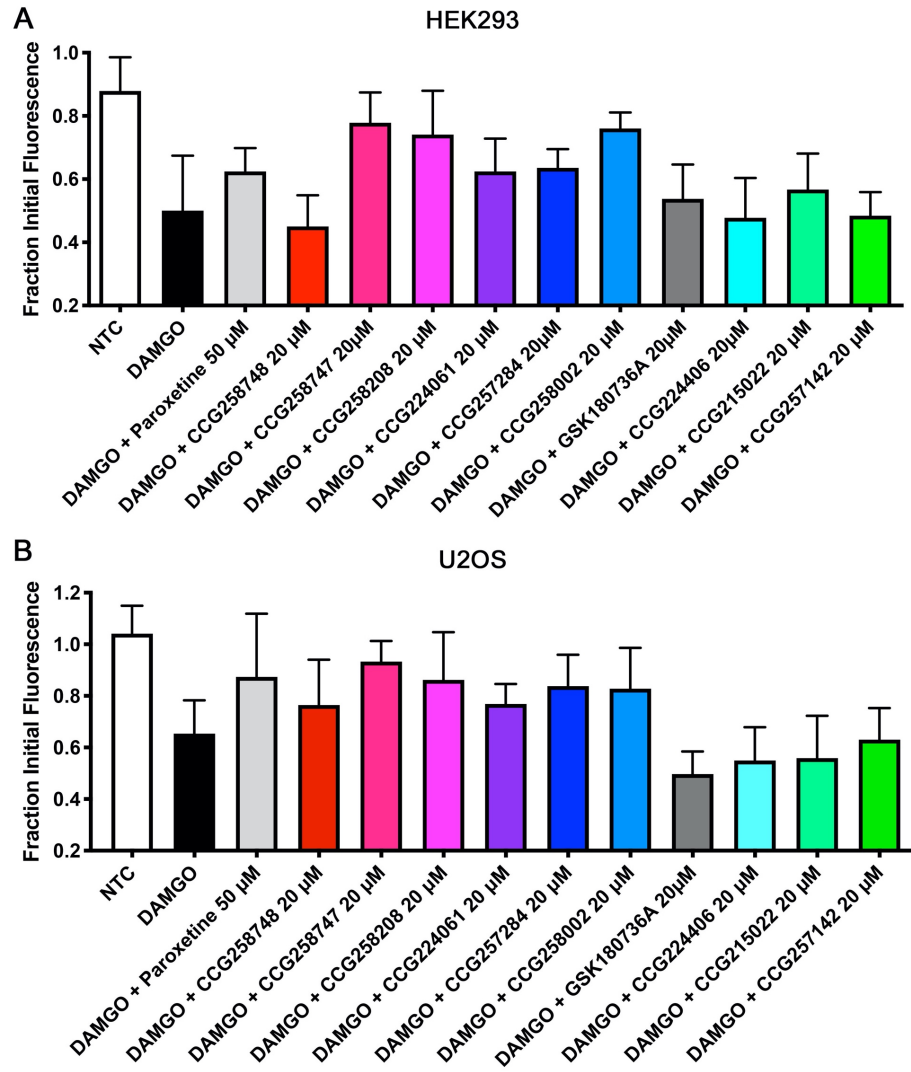
Supplementary Figure 4. Reduction of MOR internalization by GRK2 Inhibitors.
Quantitation was performed by normalizing the overall fluorescence to the initial signal for each experiment for C) HEK293 and D) U2OS cells expressing the SpH-MOR construct. Cells were pre-treated with inhibitors for at least 10 min prior to DAMGO treatment. Endpoints are at 12 min and represent an average of 20 fields per coverslip (1 coverslip per condition for HEK293 and 3 coverslips per condition for U2OS). Error bars show the standard deviation.
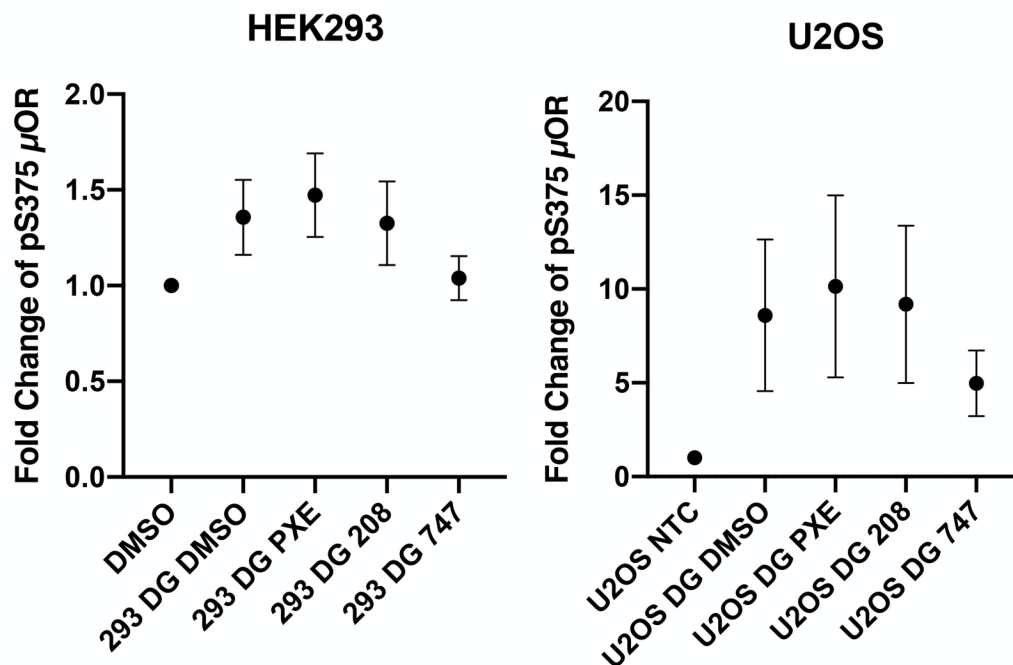
Supplementary Figure 5. Quantification of effect of CCG258747 on phosphorylation of MOR Ser375. Blots were normalized as described in methods to control for variation in total protein levels, MOR expression levels, and day-to-day variability in drug treatment. Normalized values for SpH-MOR-expressing HEK293 (left) and U2OS cells (right) are presented as mean ± range for 2 biological replicates. Cells were pretreated with DMSO, 50 µM paroxetine (PXE), 20 µM CCG258208 (208), or 20 µM CCG258747 (747), followed by DAMGO (DG). DAMGO increases receptor phosphorylation, with CCG258747 pretreatment causing minor inhibition of this effect, although it is not statistically significant via one-way repeated measures ANOVA for either HEK293 ($p = 0.269$) or U2OS cells ($p = 0.314$).